PROCEEDINGS A

royalsocietypublishing.org/journal/rspa

Research

Article submitted to journal

Subject Areas:
Fluid mechanics, geophysics, mathematical modelling

Keywords:
Topographic waves, Rossby waves, Earth rotation, fluid-solid interaction, core-mantle coupling

Author for correspondence:
Rémy Monville
e-mail:
remy.monville@univ-grenoble-alpes.fr

Topography-driven flows in magnetized planetary layers

R. Monville, D. Cébron and D. Jault

Univ. Grenoble Alpes, Univ. Savoie Mont Blanc, CNRS, IRD, Univ. Gustave Eiffel, ISTerre, 38000 Grenoble, France

While mechanical couplings between fluid and solid domains have been widely studied, their estimation remains challenging for deep planetary fluid layers with buoyancy, magnetic field, and topographic effects. Results from atmospheric or oceanic sciences are unsuitable for thick layers such as subsurface oceans of icy moons, or liquid cores of planets. Rapid rotation and/or the presence of a magnetic field in these regions may also cause difficulties. Considering a rotating and stratified fluid layer, we have developed an asymptotic local model to investigate the small-scale topographic fluid-solid coupling due to pressure or magnetic stresses. Our code unlocks several previous limitations of planetary coupling studies. Considering three-dimensional bumps, it provides the fluid stress on an electrically conducting solid (e.g. the mantle lowermost layer). We explore a wide range of parameters and boundary conditions for arbitrary topography shapes, and account for planetary curvature effects by considering a "non-traditional β-plane" approximation. Carrying out a detailed study of the wave drag mechanism, we show that the Rossby planetary waves, which are absent from recent asymptotic models, can significantly modify the boundary stress. We also show that the results are drastically different when considering 3D topographies instead of ridges.

1. Introduction

Studying geophysical flows commonly requires describing the dynamics of a stratified rotating fluid flowing along non-flat solid boundaries. This generic problem is indeed relevant for various planetary fluid layers, which can be either shallow (ocean, atmosphere) or deep (planetary liquid cores, subsurface oceans of icy moons). However, the geophysically relevant regime of vanishing viscosity makes it difficult to undertake direct simulations of such topography-driven flows.

THE ROYAL SOCIETY PUBLISHING

Additional numerical difficulties arise when considering magnetic fields (as for the Earth's liquid core) or planetary curvature (for large-scale flows) since they may require global planetary models. This long-standing fluid dynamics issue [1,2] has thus been tackled theoretically in hydrodynamic cases [3], mainly motivated by geophysical flows in the atmosphere and the ocean (see [4] for a review on topographic waves in the ocean). In the laminar regime, these studies have notably shown that flow-induced boundary stress mainly originates from the drag of topographic hydrodynamic waves, the so-called lee or orographic waves.

In planetary liquid cores, the planetary curvature cannot be neglected for large-scale flows, and the background magnetic field is a key ingredient of the liquid metal dynamics. The wave drag can then also be due to magneto-hydrodynamic (MHD) waves, such as Alfvén, torsional, or Magneto-Coriolis waves [5]. Since these waves can efficiently transport momentum and energy, they can be recovered from geophysical observations, such as geomagnetic data [6,7] or planetary rotation data [8]. Indeed, the accurate tracking of the Earth and Moon's rotations allows for constraining the coupling between the liquid core and the mantle. However, despite well-constrained values, the coupling mechanisms are still disputed (e.g., [9]). Building on pioneering articles [10,11], recent works dealt with the laminar dynamics of a stratified fluid layer, located above the convective bulk of the liquid core and below a bumpy Core-Mantle Boundary (CMB). Investigating the stress generated by the flows in this layer, these studies conclude that they may explain the observed Earth length of the day variations [12,13], or the dissipation (i.e., the imaginary part of the coupling) of the annual nutation [14]. However, these calculations have been performed under multiple (sometimes severe) assumptions, such as discarded induction and advection [14], short topography wavelength [13], or strong fluid stratification [12]. Another limitation of these models, calculated in a planar geometry, is the presence of fluxes of electric current and momentum at infinity. As a result of these fluxes, the average Coriolis and magnetic force are non-zero (even with an insulating wall) and balance the topographic stress on the solid. Direct extrapolation of these results to a spherical geometry is unacceptable from a physical standpoint, motivating us to revisit these models. Finally, these works have considered some relevant, but very specific, asymptotic limits, making their results difficult to extrapolate to other configurations or planetary cores.

Building on these recent works, our aim here is to unlock these limitations by developing a general framework for these hydromagnetic laminar flow models over a bumpy periodic topography. To do so, we combined symbolic computations and arbitrary precision algebra to extend previous theoretical models to higher (arbitrary) orders. Using the latest non-traditional β-plane approximation [15], we have also better accounted for planetary curvature effects, allowing us to consider larger-scale flows. Finally, we do not limit our model to particular asymptotic regimes, which allows exploring continuously, in the same framework, the flows in the atmospheric or oceanic regimes, but also planetary liquid cores or magneto-hydrodynamic experimental setups. We aim to gain some insight into the physical mechanisms controlling the drag in these different regimes, identifying the main waves and the dissipative effects at work.

In Section 2 we first present the geometry of the problem, the equations, and our methodology. The next section is devoted to our numerical results. We first show that we recover classical boundary layer flows. Then, we introduce topography and extend previous linear results to higher orders. We specifically investigate the effects that lead to topographic stresses on the wall, and their asymptotic limits. Section 4 begins with a discussion of the topographic waves and the associated stress. We modify the model to include some effects that are relevant for planets, such as an electrically conducting solid or a second boundary. We conclude this section with a brief discussion of the geophysical applications and the motivation to undertake new laboratory experiments.

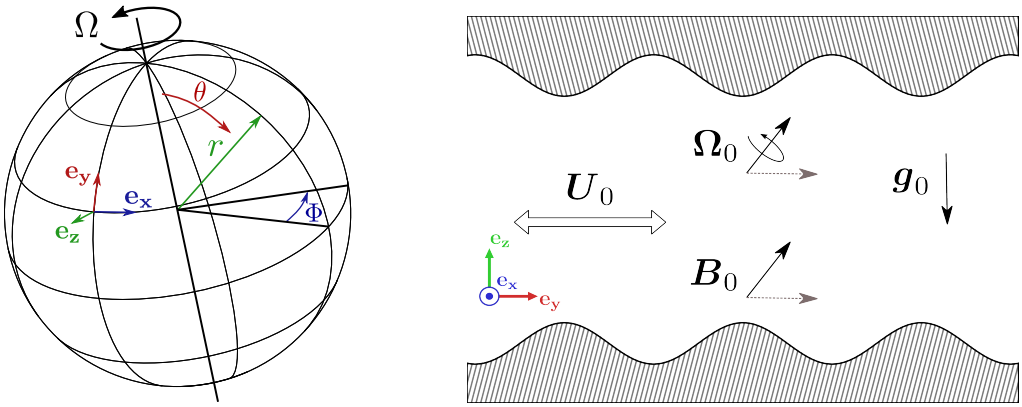

Figure 1. Perturbing the global geometry (a) by small wavelength topographies, a local Cartesian box model can be used (b), imposing a basic flow $\boldsymbol{U}_0$ and magnetic field $\boldsymbol{B}_0$ in a frame rotating at $\boldsymbol{\Omega}_0$, with the gravity vector $\boldsymbol{g}_0$.

2. Method

(a) Geometry and governing equations

We investigate in this work the boundary coupling between a planetary fluid layer and a solid domain (e.g. the solid inner core and/or the mantle). Focusing on spherical boundaries with shape perturbations that are small when compared to their typical radius R, we use a local box model. The geometry is then approximated by its tangent plane, and the problem is tackled in a periodic Cartesian frame (see Figure 1(a)). The spherical coordinate system $[\mathbf{1}_{\boldsymbol{r}}, \mathbf{1}_{\boldsymbol{\theta}}, \mathbf{1}_{\boldsymbol{\Phi}}]$ is thus converted into a local frame with $\mathbf{1}_{\boldsymbol{x}} = \mathbf{1}_{\boldsymbol{\Phi}}$, $\mathbf{1}_{\boldsymbol{y}} = -\mathbf{1}_{\boldsymbol{\theta}}$ and $\mathbf{1}_{\boldsymbol{z}} = \mathbf{1}_{\boldsymbol{r}}$. To account for the planetary rotation, we work in the frame of reference rotating at $\boldsymbol{\Omega}_0$, and buoyancy effects are due to a constant gravity $\boldsymbol{g}_0 = -g_0 \mathbf{1}_{\boldsymbol{z}}$ (Figure 1(b)).

Assuming periodicity in the x and y directions, we consider first a semi-infinite fluid, which we then extend to a fluid layer enclosed between two boundaries. In both cases, boundary shapes can be three-dimensional polychromatic bumps (Figure 2), that can be described with Fourier series

$$h(x,y,t) = z_0 + \epsilon_t \sum_j \Re\left[\mathrm{A}_j \mathrm{e}^{\mathrm{i}(\boldsymbol{k}_{H_j}\cdot\boldsymbol{r} - \omega_j t)}\right], \tag{2.1}$$

noting z_0 the boundary position without topography perturbation. We note $\boldsymbol{r}$ the position vector, and, for each topography component, A_j the amplitude, $\boldsymbol{k}_{H_j}$ the horizontal wave vector in the $x-y$ plane and ω_j the angular frequency (as required for rigid topographies studied in moving fluid frames, or for dynamical topography [16]). The relevant topography length for the flow is the one seen by the fluid along its motion along the bumpy boundary. As our basic flow is along $\mathbf{1}_{\boldsymbol{x}}$ in the following, we choose the largest topography wavelength $1/\tilde{k}$ in this direction as unit of length. This defines the non-dimensional height $\epsilon_t \ll 1$ of the topography, which is considered small to handle the topography effects in a perturbative way.

We assume the presence of a basic flow $\boldsymbol{U}_0$ and magnetic field $\boldsymbol{B}_0$, of respective typical magnitudes $\tilde{U}$ and $\tilde{B}$. In the following, we use the time unit $1/(\tilde{U}\tilde{k})$ and the magnetic field unit $\tilde{U}(\rho_r\mu)^{1/2}$, using the fluid reference density ρ_r as the density unit and noting the fluid magnetic permeability μ. Buoyancy effects are included in our model under the Boussinesq approximation. Considering a linear equation of state for the density changes, the dimensionless buoyancy $g_0\rho/(\tilde{U}^2\rho_r\tilde{k})$ is written as $a_0(z) + a$. The buoyancy anomaly a is then an unknown of the problem, and the dimensionless basic state $a_0(z)$ is characterised by the local (dimensional) Brunt-Väisälä

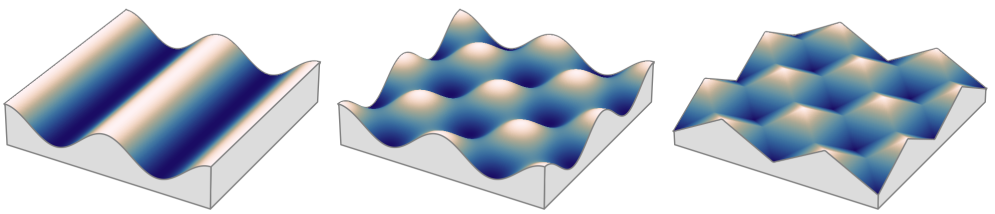

Figure 2. Typical topography handled by our code, from the simple 1D ridge shape (left) considered in previous studies [12–14], to the more complex and realistic 3D topographies considered in this work (middle: egg-box topography, right: pyramidal-egg-box topography).

frequency N through $N = \tilde{U}\tilde{k}(-g_0\partial_z a_0(z))^{1/2}$. Considering a Newtonian fluid in the rotating frame of reference, the dimensionless velocity $\boldsymbol{u}$, magnetic field $\boldsymbol{b}$ and buoyancy anomaly a are thus governed by

$$\partial_t \boldsymbol{u} + (\boldsymbol{u}\cdot\nabla)\boldsymbol{u} = -2Ro^{-1}\boldsymbol{\Omega}\times\boldsymbol{u} - \nabla p + a\mathbf{1_z} + (\nabla\times\boldsymbol{b})\times\boldsymbol{b} + Re^{-1}\nabla^2\boldsymbol{u} \tag{2.2a}$$

$$\partial_t a + (\boldsymbol{u}\cdot\nabla)a = -u_z Fr^{-2}, \tag{2.2b}$$

$$\partial_t \boldsymbol{b} = \nabla\times(\boldsymbol{u}\times\boldsymbol{b}) + Rm^{-1}\nabla^2\boldsymbol{b}, \tag{2.2c}$$

with the solenoidal constraints $\nabla\cdot\boldsymbol{u} = \nabla\cdot\boldsymbol{b} = 0$, and using the reduced pressure p which includes the centrifugal effect. Noting the fluid kinematic viscosity ν and magnetic diffusivity η, we have introduced the Froude number $Fr = \tilde{U}\tilde{k}/N = 1/\sqrt{\partial_z a_0(z)}$, the Rossby number $Ro = \tilde{U}\tilde{k}/\Omega_0$, the Alfvén number $Al = \tilde{U}\sqrt{\rho_r\mu}/\tilde{B}$, the magnetic Reynolds number $Rm = \tilde{U}/(\eta\tilde{k})$, and the Reynolds number $Re = \tilde{U}/(\nu\tilde{k})$. We also define the Lehnert number $Le = RoAl^{-1}$. In the following, we only consider the case of uniform stratification $a_0 \propto z$ and Fr is thus constant.

For a topography with a large length scale, the dimensionless parameter $\chi = 1/(\tilde{k}R)$ is also important. Indeed, the regime $\chi \ll 1$ imposes that the local model includes curvature effects from the spherical geometry. For such perturbations, $\boldsymbol{\Omega}$ is no longer considered constant but is rather varying as

$$\boldsymbol{\Omega} = (\cos\theta + \chi y\sin\theta)\mathbf{1_z}, \tag{2.3}$$

which is relevant for thin fluid layers [17]. For deeper layers, the so-called non-traditional β-plane includes, in addition, a similar linear variation $(\sin\theta - 2\chi y\cos\theta)\mathbf{1_y}$ for the tangential component [18]. It violates $\nabla\cdot\boldsymbol{\Omega} = 0$, as well as the conservation of angular momentum or potential vorticity [15]. To solve this issue, an additional term $2\chi z\cos\theta\mathbf{1_z}$ is then required, related to the vertical variation of the radial component of $\boldsymbol{\Omega}$, which gives [15]

$$\boldsymbol{\Omega} = \left[0, \quad \sin\theta - 2\chi y\cos\theta, \quad (1+2\chi z)\cos\theta + \chi y\sin\theta\right]^{\mathsf{T}}. \tag{2.4}$$

These approximations introduce linear dependencies in the equations. We then take the curl of the equation (2.2*a*), which removes the unknown pressure. This defines the β effect, the terms that depend linearly on y and z being neglected. At this point, we need to remove two excess equations due to the solenoidal constraint on $\boldsymbol{B}$ and $\boldsymbol{U}$. We take out one of the horizontal equations for each of the induction and vorticity equations, depending on the orientation of the horizontal wave vector. If k_x and $k_y \neq 0$ we can choose any of them. If $k_x \neq 0$ and, $k_y = 0$ we remove the equation along x and vice versa to respect the symmetry of the problem. In the end, we find the pressure field, resolving the component of the equations 2.2*a* aligned with the base flow.

While the velocity and the density unknowns are only required in the fluid domain, the magnetic field has also to be obtained in the solid. When it is insulating, the magnetic field $\boldsymbol{b}$ can be obtained from a scalar potential ψ using $\boldsymbol{b} = -\nabla\psi$ and $\nabla^2\psi = 0$. Electrically conducting domains at rest, of magnetic diffusivity η_s, are also considered in the following, such that $\boldsymbol{b}$ is governed by the diffusion equation

$$\partial_t \boldsymbol{b} = \tilde{\eta} Rm^{-1} \nabla^2 \boldsymbol{b}, \tag{2.5}$$

with $\tilde{\eta} = \eta_s/\eta$ the ratio of fluid and solid (η_s) magnetic diffusivities.

The dynamical equations are then complemented by boundary conditions. The kinematic one $\boldsymbol{u}\cdot\nabla F|_{z=h} = -\partial_t F|_{z=h}$, with the boundary surface $F(x,y,z,t) = z - h(x,y,t)$, reduces to $\boldsymbol{u}\cdot\boldsymbol{n} = 0$ for steady boundaries, with $\boldsymbol{n} = \nabla F/|\nabla F|$ the unit normal vector. This ensures that the fluid and the boundary move consistently and suffices for inviscid fluids. More conditions for the tangential components of $\boldsymbol{u}$ are required in the general case, such as the no-slip condition $(\boldsymbol{u} - \boldsymbol{u_h})\times\boldsymbol{\nabla} F|_{z=h} = \boldsymbol{0}$ with $\boldsymbol{u_h}$ the velocity of the solid, or the stress-free condition $(\boldsymbol{\sigma}\cdot\boldsymbol{n})\times\boldsymbol{n}|_{z=h} = \boldsymbol{0}$, with the viscous stress tensor $\boldsymbol{\sigma} = Re^{-1}[\nabla\boldsymbol{u} + (\nabla\boldsymbol{u})^\top]/2$. Similarly, the magnetic field continuity $\boldsymbol{b}|_{z=h^-} = \boldsymbol{b}|_{z=h^+}$ is sufficient for insulating solid domains, but in the general case, it must be complemented by continuity conditions on the tangential components of the electrical field. For steady topographies, this continuity condition reads

$$\boldsymbol{n}\times[(\nabla\times\boldsymbol{b}) - Rm\,(\boldsymbol{u}\times\boldsymbol{b})]|_{z=h^-} = \boldsymbol{n}\times[\tilde{\eta}(\nabla\times\boldsymbol{b})]|_{z=h^+}\,, \tag{2.6}$$

where $z = h^-$ is in the fluid, and $z = h^+$ is in the solid.

(b) Fluid efforts on solid boundaries

Through the pressure, electromagnetic and viscous forces, the flow generates stresses on the boundary. Neglecting viscosity, the force $\boldsymbol{F}$ on the solid reduces to

$$\boldsymbol{F} = \int_S p\boldsymbol{n}\,\mathrm{d}S + \int_V (\nabla\times\boldsymbol{b})\times\boldsymbol{b}\,\mathrm{d}V, \tag{2.7}$$

with $\boldsymbol{n}$ the normal vector pointing inward of the solid, S the fluid-solid boundary surface and V the solid volume. The Lorentz force can also be obtained by integration on a closed surface [9]), writing it as $(\nabla\times\boldsymbol{b})\times\boldsymbol{b} = \nabla\cdot\boldsymbol{\sigma^M}$, with the Maxwell stress tensor $\sigma^M_{i,j} \equiv b_i b_j - (b^2/2)\delta_{i,j}$ and the Kronecker symbol $\delta_{i,j}$. Equation (2.7) is thus transformed into

$$\langle\boldsymbol{F}\rangle = \frac{1}{S}\left(\int_S p\boldsymbol{n}\,\mathrm{d}S + \oint_{S_2}\left((\boldsymbol{n}\cdot\boldsymbol{b})\boldsymbol{b} - \frac{1}{2}b^2\boldsymbol{n}\right)\mathrm{d}S\right), \tag{2.8}$$

with S_2 the closed surface of the volume V. To estimate the stress in the box model, the local normal vector is expanded as

$$\boldsymbol{n} = \sum_{m=0}\epsilon_t^m\boldsymbol{n}_m = \left[\epsilon_t\partial_x h(x,y) + \mathcal{O}(\epsilon_t^3), \epsilon_t\partial_y h(x,y) + \mathcal{O}(\epsilon_t^3), 1 + \mathcal{O}(\epsilon_t^2)\right]^\mathsf{T}. \tag{2.9}$$

The boundary stress (2.8) induced by the topography perturbation is of the order ϵ_t^2, which requires a priori a challenging second-order calculation. For the tangential stress on the solid side, it appears that it can be obtained from simpler first-order linear solutions. The form of the horizontal component of the normal vector (2.9) (which has no zeroth order), allows us to obtain the second-order tangential pressure stress from the linear solution [12,13]. This can easily be extended to higher orders (e.g. order 2 solutions provide the tangential pressure stress at order 3).

(c) Basic states and perturbative expansions

Considering an imposed basic state for $\epsilon_t = 0$, we aim to calculate the perturbations due to the topography. A direct integration of the dynamical equations is then possible, using for instance a spectral numerical method, but it would not allow us to cope with planetary values for the

control parameters. Instead, we follow an alternative approach, linearising the equations with perturbative expansions of the non-linear terms. The basic flow $\boldsymbol{u}_0$ is written as $\boldsymbol{u}_0 = \boldsymbol{u}_{su} + \tilde{\boldsymbol{u}}$, where $\tilde{\boldsymbol{u}}$ is a small departure from a uniform steady flow $\boldsymbol{u}_{su}$. Similarly, the basic magnetic field $Al^{-1}\boldsymbol{b}_0$ is written as $\boldsymbol{b}_0 = \boldsymbol{b}_{su} + \tilde{\boldsymbol{b}}$, where $\boldsymbol{b}_{su}$ is a uniform steady magnetic field, with

$$\tilde{\boldsymbol{u}} = \sum_{n=1} \epsilon_v^n \tilde{\boldsymbol{u}}_n, \quad \tilde{\boldsymbol{b}} = \sum_{n=1} \epsilon_v^n \tilde{\boldsymbol{b}}_n. \tag{2.10}$$

The perturbations from the basic state are obtained with the double-perturbation expansion

$$\boldsymbol{u} = \boldsymbol{u}_0 + \sum_{m,n=0} \epsilon_t^m \epsilon_v^n \boldsymbol{u}_{m,n}, \quad \boldsymbol{b} = Al^{-1}\boldsymbol{b}_0 + \sum_{m,n=0} \epsilon_t^m \epsilon_v^n \boldsymbol{b}_{m,n}, \quad a = \sum_{m,n=0} \epsilon_t^m \epsilon_v^n a_{m,n}, \tag{2.11}$$

where $\boldsymbol{u}_{0,0} = \boldsymbol{b}_{0,0} = \boldsymbol{0}$ and $a_{0,0} = 0$. Introducing the ansatz (2.11) in the dynamical equations, we get a hierarchy of linear forced problems that can be integrated order by order. We use the same double perturbation expansion for the pressure in the calculation of the surface stress. We write the unknown perturbations $(\boldsymbol{u}_{m,n}, \boldsymbol{b}_{m,n}, a_{m,n})$ as a sum of harmonic plane waves of wave vector $\boldsymbol{k}^{(j)}$ and pulsation ω_j. For the part of the flow forced by the non-linearities, ω_j and $\boldsymbol{k}^{(j)}$ are given directly by the terms of previous orders. A second part of the flow arises from the boundary conditions, which give the horizontal part $(k_x^{(j)}, k_y^{(j)})$ of $\boldsymbol{k}^{(j)}$. For each $(k_x^{(j)}, k_y^{(j)})$, $k_z^{(j)}$ is obtained from the (homogeneous) dynamical equations.

A relevant basic state for planetary studies is provided by the solid body rotation around $\boldsymbol{\Omega}_0$ in the spherical geometry, leading to a uniform and steady basic flow $\boldsymbol{u}_0 = \sin\theta \mathbf{1}_{\boldsymbol{x}}$ in the local model. We can also consider an oscillating flow, which is appropriate for tidal flows or motions forced by precession/nutation [14,19]. For the sake of simplicity, the basic magnetic field is considered here to be uniform and steady in each local box model, varying in angle and magnitude as a function of the position of the local model with respect to the global geometry (e.g. to account for a dipolar field).

(d) Numerical method

At each order, the perturbed unknowns $(\boldsymbol{u}_{m,n}, \boldsymbol{b}_{m,n}, a_{m,n})$ are searched as plane wave series forced by the previous order (e.g. the basic state) and boundary conditions. In this study, we aim to go beyond the linear solution. The double perturbative expansion (2.11) has then to be obtained at high order, yielding higher accuracy and enabling the investigation of weakly non-linear effects.

The solution is expressed as the sum of exponentials $\exp[\mathrm{i}(k_x x + k_y y + k_z z - \omega t)]$. Introducing this ansatz in equations (2.2), we obtain a linear system $\boldsymbol{AX} = \boldsymbol{b}$, which is non-homogeneous for the orders $m + n \geq 2$ (*i.e.* $\boldsymbol{b} \neq \boldsymbol{0}$, where $\boldsymbol{b}$ consists in the non-linear terms arising from previous orders). The homogeneous part of the solution is obtained by considering separately each horizontal harmonics. Ensuring the existence of non-zero solutions, the zero determinant constraint provides the required values of $k_z^{(j)}$ as the roots of a polynomial whose degree depends on the number of boundary conditions. For each $k_z^{(j,k)}$, we calculate the associated non-zero solution(s) $\boldsymbol{K}_{jk}$. The eigenvalues $k_z^{(j,k)}$ can be multiple. In such a case, they yield several solutions $\boldsymbol{K}_{jk}$. We consider in the following that the list $(k_z^{(j,k)})$ contains all k_z, even identical ones, and their associated solution $\boldsymbol{K}_{jk}$. The homogeneous solution vector is thus written as

$$\sum_j \left[\exp[\mathrm{i}(k_x^{(j)} x + k_y^{(j)} y) \sum_k \left(C_{jk} \boldsymbol{K}_{jk} \exp(\mathrm{i} k_z^{(j,k)} z) \right) \right]. \tag{2.12}$$

For the particular solutions, k_z is obtained directly from the expression of the non-linear terms. It turns out that these k_z are not eigenvalues of $\boldsymbol{A}$, and consequently, we can solve the linear system $\boldsymbol{AX} = \boldsymbol{b}$. Finally, adding the particular and homogeneous solutions, the constants C_{jk} are obtained from the boundary conditions.

The calculation involves a host of k_z wavenumbers, which results in very large expressions. To tackle this difficulty and the extreme values of the dimensionless parameters, we combine

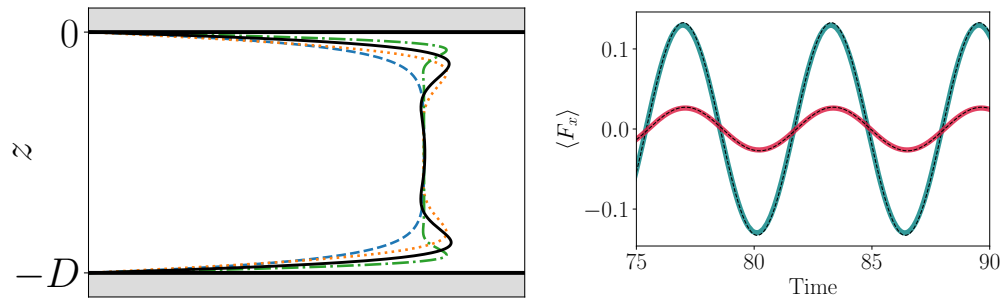

Figure 3. (a) Illustrating case of Stokes-Ekman-Hartmann flow between no-slip planes, at the order ϵ_v^2. Parameters: $Al = 0.008$, $Rm = 12.5$, $Ro = 2 \times 10^{-5}$, $Fr = 0$, $Re = 20$, $\omega = 5 \times 10^5$, $D = 7 \times 10^{-3}$, $\chi = 0$, $\epsilon_v = 0.1$, $\tilde{\eta}^{-1} = 0$, with $\boldsymbol{u}_0 = \epsilon_v \cos(\omega t)\mathbf{1}_x$ and $\boldsymbol{b}_0 = \mathbf{1}_z$. Compares u_x (black line) to Ekman (dotted orange), Stokes (dashed-dotted green) and Hartmann (dashed blue) flows. (b) Comparison of tangential stresses on a stress-free bumpy boundary (without magnetic field and rotation), obtained with our code (dashed) in a semi-infinite fluid layer, and with finite element DNS calculations (solid) using a second boundary at $z = -D = -4$, which is flat and no-slip, moving at $\boldsymbol{u}_0$. The blue line represents the total stress and the red line is the viscous one. Parameters: $Fr = 0.1$, $Re = Re_a = 1$, $u_0 = \sin t$, $\tilde{\eta}^{-1} = 0$, $h = 0.05 \sin x$.

symbolic and arbitrarily precise calculations and perform linear algebra automatically. In our code, written in Python, the symbolic calculations are achieved using the "Sympy" package [20]. Extreme parameters can lead to badly conditioned matrices. Handling these matrices requires high-precision calculations, which are performed with the arbitrary precision package "mpmath" [21]. The code is then fast enough to allow systematic exploration of the parameter range. Typically, calculation at order 4 necessitates about ten hours on one computing core, for the simplest case of a topography with one harmonic, for an inviscid fluid and an insulating mantle.

3. Results

We first test our unconventional numerical method against standard boundary-layer flows and previously obtained linear solutions of topographic core-mantle coupling. We then obtain the maximum bump height ϵ_t for this approach to be valid. The physics of the hydromagnetic topographic coupling is then explored, characterising the regimes of interest.

(a) Standard boundary layers and linear flows at a bumpy CMB

Fluid-solid interactions are typically found in boundary layers, which are well-known and include a limited number of physical ingredients. In the frame of our approach, we have checked that standard solutions on flat boundaries are easily retrieved, such as the Ekman, Hartmann and Stokes boundary layer flows. The coloured lines illustrate in Figure 3(a) these classical flows, which agree perfectly with the theory (not shown). We also calculate more complex boundary layers on a flat wall. As an illustrating case, we consider a rotating and magnetised viscous fluid oscillating along $\mathbf{1}_x$ between two no-slip planes. In Figure 3(a) we show one solution that includes weakly non-linear effects of order 2 (that are dominant in Blasius boundary layers).

Having validated the main physical ingredients of the dynamical equations on flat boundaries, one can now consider the presence of topography. To do so, a finite element model with a bumpy boundary has been developed to perform direct numerical simulations (DNS). To control numerical diffusion effects due to the mesh grid, this model uses finite diffusivities, and we thus consider in this section a non-zero viscous term in the Navier-Stokes equation (2.2*a*) as well as a diffusive term $Re_a^{-1}\nabla^2 a$ in the right-hand side of the density equation (2.2*b*). A simple benchmark

	Braginsky (1998) [11]	Buffett (2010) [14]	Glane & Buffett (2018) [13]	Jault (2020) [12]	This work
Lorentz force	✓	×	✓	✓	✓
Advection	×	×	✓	✓	✓
3D bumps	×	✓	×	$\times^{(a)}$	✓
β-plane	$\checkmark^{(b)}$	×	×	$\checkmark^{(b)}$	✓
Any tilt of $\boldsymbol{B}$ and $\boldsymbol{\Omega}$	×	×	×	$\checkmark^{(c)}$	✓
Weakly non-linear	×	×	×	×	✓
Two boundaries	$\checkmark^{(d)}$	×	×	×	✓
Non-uniform U, B, ρ	×	×	×	×	✓
Asymptotic limits	$Rm \ll Al^2 Ro^{-1}$			$Fr \ll 1$, $Ro \ll 1$ $Rm \ll Al^2 Fr^{-2}$	

(a) Preliminary results (see Appendix C of [12])

(b) $\boldsymbol{\Omega}$ is present only via its vertical component

(c) Only 2 orientations of $\boldsymbol{B}$ (vertical and horizontal)

(d) Flat second boundary; our code can consider one or two (possibly bumpy) boundaries

Table 1. Summary of the approximations used in previous studies

case is then provided by the oscillating flow in a stratified fluid along a 2D topography, which leads to a bounded 2D flow (Stokes boundary layer). To compare with our results in a semi-infinite fluid domain, we use in the DNS a far enough no-slip second boundary at $z = -D$, which is flat and moves at the velocity $\boldsymbol{u}_0$. As shown in Figure 3(b), the viscous and total stresses (viscous and pressure) are in excellent agreement. By contrast with flat boundaries, the viscous force along the basic flow direction is non-zero for a stress-free bumpy boundary. The topography indeed allows the normal viscous stress to generate a non-zero horizontal viscous drag.

Thereafter, we consider the asymptotic limit $Re^{-1} = Re_a^{-1} = 0$. This limit has the advantage of removing the associated boundary layers. Indeed, their presence imposes a severe upper bound on the maximum topography height ϵ_t that can be considered in our code (the perturbation approach requires ϵ_t to be smaller than the boundary layer thickness). By contrast with DNS, the perturbation approach enables handling the MHD topographic coupling in the planetary-relevant inviscid limit. This has been exploited by previous studies that have considered linear solutions under various hypotheses, to simplify the equations or obtain analytical results. For instance, we have reproduced (not shown) previous non-magnetic atmospheric [22] and oceanic [4] results, as well as classical hydromagnetic wave dispersion relations [5]. Furthermore, we have successfully validated our topography-driven MHD flows against previous works [11–13] by considering the various assumptions summarised in Table 1.

For the quite large CMB topography wavelength of ~ 600 km considered here, figure 4(a) compares our topographic stress results with studies that are also using β-plane approximations, *i.e.* Jault (2020) [12] and Braginsky (1998) [11]. Because of the assumptions of these two previous works ($Rm^{-1} \gg RoAl^{-2}$ for [11], $Rm^{-1} \gg Al^{-2}Fr^2$ for [12]), these three models differ in the limit of small Rm^{-1} but agree for large Rm^{-1} values, notably at Earth's core parameters. For large topography wavelength, the β-terms are crucial, as illustrated in figure 4(b) (compare dashed black and red curves). In a certain range of Rm, the model built in the limit $Fr \ll 1$ allows however to retrieve the correct boundary stress, even without the β-plane terms (compare orange and dashed black curves).

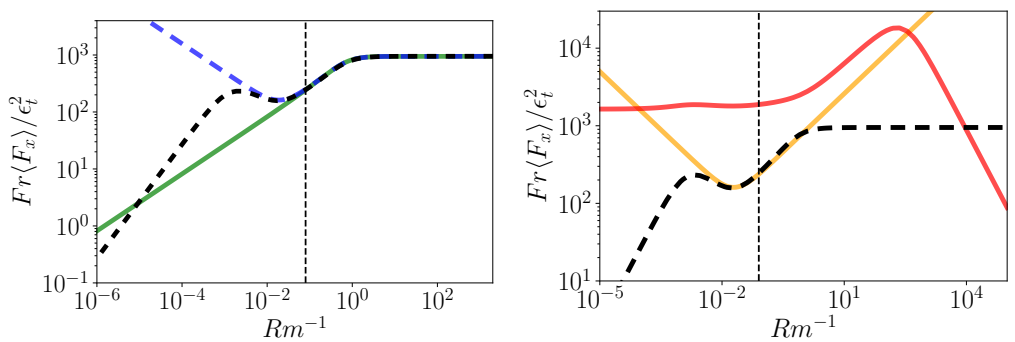

Figure 4. Stress as a function of Rm^{-1} (the vertical dashed line shows a realistic geophysical value $Rm = 12.5$). (a) Comparison of our model with the ones of Jault (2020) [12] (dashed blue) and Braginsky (1998) [11] (green) which both include β-plane effects. (b) Comparison of $\langle F_x\rangle$ calculated with (black dashed) and without β terms ($\chi \equiv 0$, red and orange solid). The limit $Fr \ll 1$ (orange) allows us to recover the estimate obtained with the β term for Rm^{-1} in $0.01 - 1$. Parameters: $Ro = 1.37 \times 10^{-5}$, $Al = 2.24 \times 10^{-2}$, $\chi = 2.86 \times 10^{-2}$, $\boldsymbol{u}_0 = \mathbf{1}_x$ $\boldsymbol{b}_0 = \mathbf{1}_z$, $\theta = \pi/4$, $\tilde{\eta}^{-1} = 0$ and $h = \epsilon_t \sin x$.

(b) Beyond linear flow solutions

Higher-order solutions are desired for their better accuracy, possibly allowing larger topography heights, but also because they can quantify the validity limits of lower-order solutions. Yet, the associated numerical cost can quickly become prohibitive. Figure 5(a) shows indeed that the number of harmonics involved in the calculation grows exponentially with the order. Moreover, this figure also shows that the number of harmonics can already be quite large at the lowest order $m = 1$ for the topography height. Having optimised our implementation, our code is now typically capable of calculating order 3 hydromagnetic solutions with 3D topographies (requiring ~ 1000 harmonics). One can now use these higher-order solutions to quantify convergence with the order. For instance, looking at the residual error on the non-penetration boundary condition, figure 5(b) shows that our perturbation-based method only converges below a certain value ϵ_t^c of ϵ_t, and ϵ_t^c being nearly independent of m. But the error can actually be already quite large for $\epsilon < \epsilon_t^c$, the case $N = 20\Omega$ of [13] requires an order $m = 3$ to reduce the error around 10%. These convergence issues are actually related to the smallest length scale of the problem (vertical dashed lines), either originating from the geometry or from the values of $k_z^{(j,k)}$. In the case considered in Figure 5(b), this limit is related to stratification through $\max(k_z^{(j,k)})$, which is proportional to Fr^{-1} for strong stratification [12]. When $\epsilon < \epsilon_t^c$, Figure 5(b) also confirms that higher orders allow the use of higher topographies for the same accuracy (e.g. one order of magnitude larger between orders $m = 1$ and $m = 3$). As allowed by our approach, considering such larger topography heights may be important to account for geophysical observations [12]. As an explicit illustration of the accuracy gain provided by higher orders, Figure 6 compares the flow at order 1 and 4 for a typical hydromagnetic calculation. The flow is notably modified near the boundary to better ensure the non-penetration boundary condition.

(c) Topographic stress regimes

Thanks to our efficient numerical method, we can perform a systematic survey of hydromagnetic topographic stresses for different topography shapes and wavelengths. We exhibit various regimes and sharp transitions when plotting the stress F_x as a function of Ro and the interaction parameter Rm/Al^2 (figure 7), keeping the Lehnert number $Le = Ro/Al$ constant. The stress

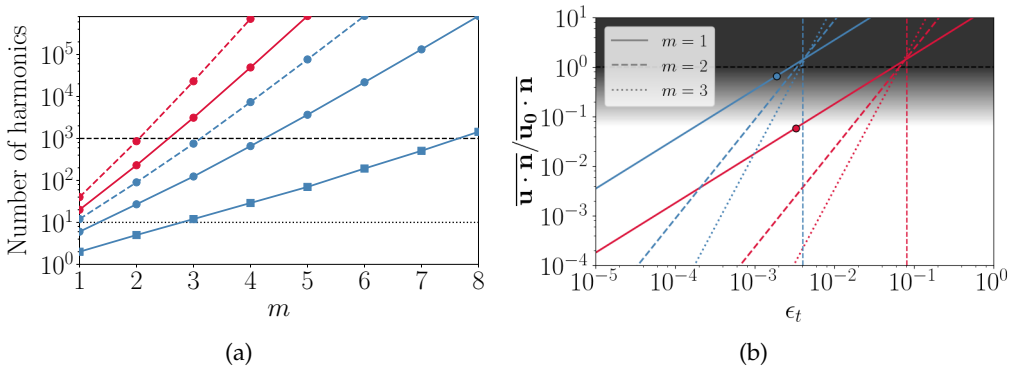

Figure 5. (a) Number of harmonics vs order m (at $n=0$, see equation 2.11), for a steady basic flow $\boldsymbol{u}_0=\mathbf{1}_x$ and an inviscid semi-infinite fluid (blue) or a viscous fluid between two boundaries (red). Topography is either a ridge ($h=\cos(k_x x)$, solid lines) or 3D ($h=\cos(k_x x)\cos(k_y y)$, dashed). The basic magnetic field is either zero (squares) or not (circles, $\boldsymbol{b}_0=\mathbf{1}_z$). Horizontal lines: typical values for previous works [12–14] based on linear perturbations (dotted) and for one-day computations using our code on a laptop (dashed). (b) The normalised mean residual for the boundary condition $\boldsymbol{u}\cdot\boldsymbol{n}=0$ versus ϵ_t for three different orders of topography perturbation m (at $n=0$). Circles: typical cases [13] with $N=20\Omega$ (blue) and $N=\Omega$ (red). Vertical dashed lines: smallest length scale at $m=1$. Grey shading: high residual or diverging series. Parameters : see table 2, with $\tilde{\eta}^{-1}=0$.

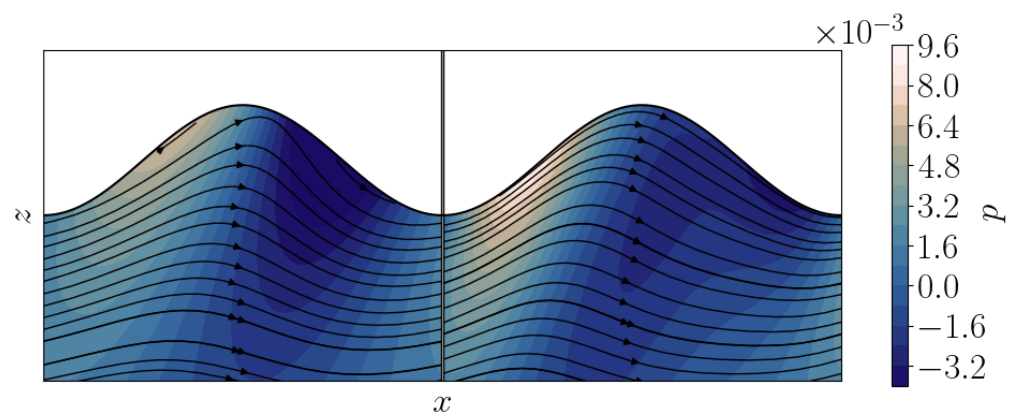

Figure 6. Flow streamlines and pressure field at order 1 (left) and order 4 (right). Parameters: $Al=0.022$, $Rm=12.5$, $Ro=Fr=1.37\times10^{-5}$, $Re^{-1}=0$, $\chi=\theta=0$, $\epsilon_t=6\times10^{-3}$ with an insulating solid ($\tilde{\eta}^{-1}=0$) with 2D topography models $z=-\epsilon_t\cos(x)$, $\boldsymbol{u}_0=\mathbf{1}_x$ and $\boldsymbol{b}_0=\mathbf{1}_z$.

on the boundary is due to dissipative processes, but also to radiated waves, which exist for specific control parameters. Considering the Earth's core radius $R=3486$ km and the topography wavelengths $\tilde{k}^{-1}=5$ km, we first show (top figures) the stress for a ridge topography, with $\chi=0$ (f-plane, figure 7(a)) and with traditional β-plane effects (figure 7(b)). Then we investigate 3D topography (bottom figures), with either traditional or non-traditional β-plane approximations (respectively, figure 7(c) and 7(d)). In these figures, typical values for the Earth's core and oceans (see Table 2) are also indicated to illustrate the strong influence of the magnetic field on the stress (even with insulating boundaries). For oceanic application ($R=6371$ km) the topography wavelengths is $\tilde{k}^{-1}=9$ km since χ is fixed.

Parameters	$\tilde{k}^{-1} = 5$ km	$\tilde{k}^{-1} = 100$ km	Glane & Buffett (2018) [13]
Ro	2.74×10^{-4}	1.37×10^{-5}	4.32×10^{-4}
Fr	2.74×10^{-4}	1.37×10^{-5}	2.16×10^{-5} - 4.32×10^{-4}
Rm	6.25×10^{-1}	12.5	9.92
Al	2.24×10^{-2}	2.24×10^{-2}	8.86×10^{-2}
χ	1.43×10^{-3}	2.86×10^{-2}	0

Table 2. Parameters used in this study (typical for Earth core-mantle boundary), and in Glane & Buffett (2018) [13].

Figures 7 show sharp changes of the stress as a function of Ro and Rm/Al^2. We delineate regions in the parameter space, which each corresponds to the propagation of different kinds of MHD waves. We have identified the waves that contribute the most to the total stress (see section 3(d) and Supp. Mat.) and reported their names in figure 7. The parameter space is divided in two, on either side of $Rm/Al^2 = 1$ (black dashed line). We characterize these regions by considering the asymptotic limits $Rm/Al^2 \gg 1$ (negligible diffusion in the induction equation, *i.e.* ideal MHD) and $Rm/Al^2 \ll 1$ (negligible role of the magnetic field *i.e.* hydrodynamic case). This helps us to find the limits of the major regions using the dispersion relation of waves (for further details, see section 3(c)).

In the hydrodynamic limit, the limit of propagation of inertial gravity waves (red dotted line) can be written as

$$Ro > 2\cos\theta \tag{3.1}$$

in our limit of interest $Fr < 1$. We find significant stress in the presence of the internal waves that are almost independent of Ro. In the opposite case $Ro < 2\cos\theta$, for which the waves are evanescent, the stress is negligible.

In the MHD case $Rm/Al^2 \gg 1$, the vertical dashed red line,

$$Al = 2k_H Fr^{-1}\cos\theta, \tag{3.2}$$

corresponds to the transition between MAC (Magneto-Archimede-Coriolis) waves on the left and internal waves, for $Fr \ll 1$ and $Ro \gg 1$. This gives the transition from Alfvén waves to internal waves. For $Ro \ll 1$, magnetic effects are important for the stress when the Elsasser number $\Lambda = RoRmAl^{-2}\cos\theta$, which compares the magnetic and Coriolis forces, is larger than 1 (dashed-dotted line). In this domain, the stress indeed increases as Al^{-1}, a measure of the magnetic field strength.

A new family of waves, the Rossby waves, arises in the β-plane model (compare 7(b) to 7(a)). In the hydrodynamic case, the force becomes driven by Rossby waves (modified by the stratification) when

$$k_H^2 Ro < 2\chi\sin\theta, \tag{3.3}$$

shown by the dotted blue line. This hydrodynamic regime now extends to $\Lambda = 1$. In this domain, the stress increases directly with $Ro^{-1/2}$ and is independent of the magnetic field. A domain of evanescent inertial gravity waves remains between the regions where Rossby and internal waves propagate. For $\Lambda > 1$, the Rossby waves are significantly modified by the magnetic field, hence named Rossby-MAC, yielding a stress that is weaker than in the f-plane case.

In the case of 3D topography, these Rossby-MAC waves only exist in a finite range of Ro (figures 7(c) and 7(d)). This extent of this domain is significantly shrunk for $\boldsymbol{\Omega}$ given by equation 2.4 (compare figure 7(c) calculated with equation 2.3 for $\boldsymbol{\Omega}$ and figure 7(d)). This domain is bounded by

$$k_H^2 Ro = \chi\sin\theta\left[1 \pm \sqrt{1 - \varpi(Fr|k_y|k_H/\chi)^2}\right], \tag{3.4}$$

with $\varpi = 1$ and $\varpi = 9$ when respectively using equations (2.3) and (2.4). The derivation of these limits is detailed in Supp. Mat. and are found imposing a zero determinant for the dynamical equations, using the calculated k_z values. Equation (3.4) illustrates the importance

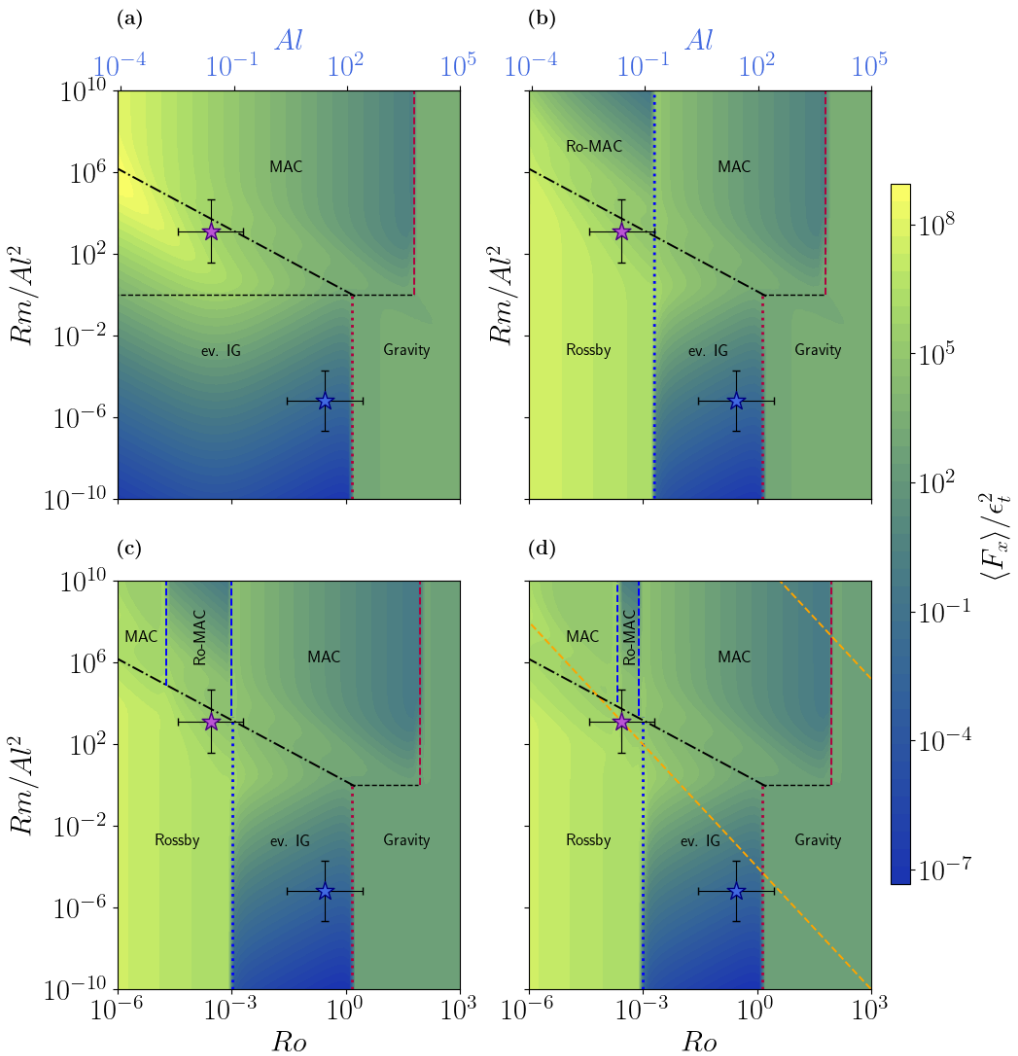

Figure 7. Normalised stress (colours) as a function of interaction parameter Rm/Al^2 and Ro at $\theta = \pi/4$ for (top) a ridge $h = \epsilon_t \cos x$, or 3D topography (bottom). Figure (a) is with $\boldsymbol{\Omega} = \cos\theta \mathbf{1}_z$ (f-plane) and $\boldsymbol{b}_0 = -\cos\theta \mathbf{1}_z$. In figure (b) $\boldsymbol{\Omega} = (\cos\theta + \chi \sin\theta)\mathbf{1}_z$, and (c,d) are with non-traditional β-plane approximation. Figures (b, c, d) have a magnetic field $\boldsymbol{b}_0 = \sin(\theta)/2\mathbf{1}_y - \cos\theta \mathbf{1}_z$ (equation 2.4). The stress is shown $\chi = 0.0014$, i.e. $\tilde{k}^{-1} = 5$ km for the core and $\tilde{k}^{-1} = 9$ km for the ocean. The stars represent the Earth's core (purple) and ocean (blue). The bounds for internal waves are the red dotted line (equation 3.1) and the dashed one (equation 3.2). The bounds for Rossby waves are the blue-dotted line (equation 3.3) and the dashed blue ones (equation 3.4). The dashed-dotted black line is $\Lambda = 1$. The orange dashed lines are $Rm = 10^{15}$ and $Rm = 0.625$, for which figures 9(a) and 9(b) respectively, have been obtained. Within each zone, the type of wave that contributes the most to the total stress is written. Parameters: $\tilde{\eta}^{-1} = 0$, $\boldsymbol{u}_0 = \mathbf{1}_x$, $Le = 0.0122$ (see Table 2 for others parameters at corresponding wavelengths).

of 3D topographies ($k_y \neq 0$) and density stratification ($Fr \neq 0$) when considering $\chi \neq 0$. We have also investigated a larger topography wavelength $\tilde{k}^{-1} = 100$ km for the core ($\chi = 0.0287$, leading to $\tilde{k}^{-1} = 183$ km for the ocean). Figures 8(a) and 8(b) can respectively be compared with figures 7(a) and 7(b). We find that in the simplest case (f-plane, ridge topography) our results are mainly unchanged. The domain of MAC waves extends to a weaker magnetic field (larger Al) with

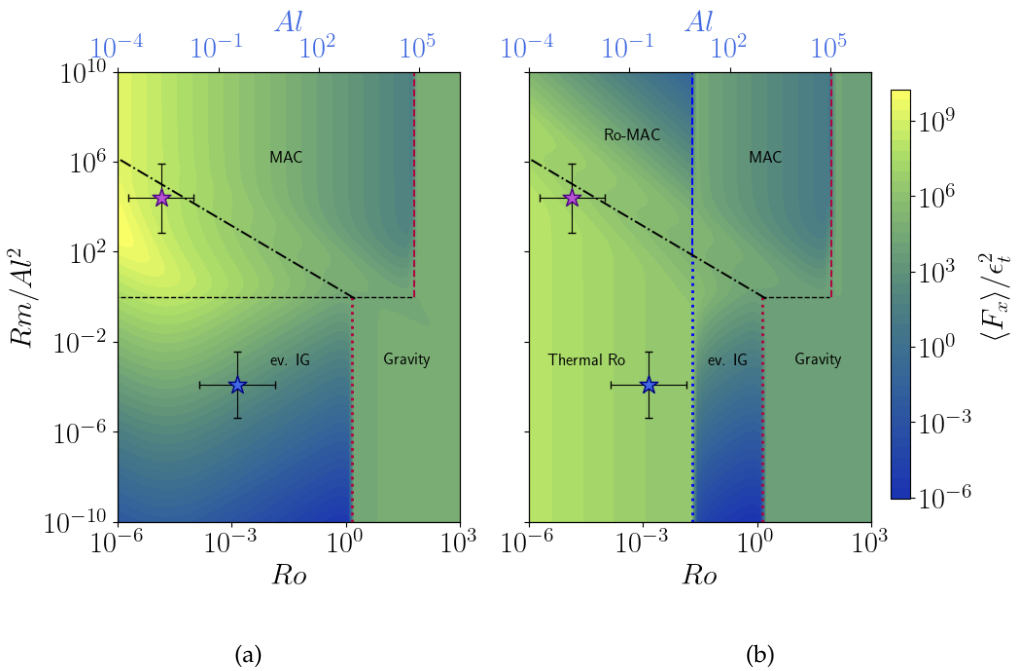

Figure 8. Normalised stress (colours) as a function of interaction parameter Rm/Al^2 and Ro at $\theta = \pi/4$ for (left) a ridge topography $h = \epsilon_t \cos x$, $\boldsymbol{b}_0 = -\cos\theta \mathbf{1}_z$ and $\boldsymbol{\Omega} = \cos\theta \mathbf{1}_z$ (f-plane), and (right) a 3D topography $h = \epsilon_t \cos x \cos y$,$\boldsymbol{b}_0 = \sin(\theta)/2\mathbf{1}_y - \cos\theta \mathbf{1}_z$ and non-traditional β-plane (equation 2.4). The stress is shown for $\chi = 0.0287$, i.e. $\tilde{k}^{-1} = 100$ km for the core and $\tilde{k}^{-1} = 183$ km for the ocean. The stars represent the Earth's core (purple) and ocean (blue). Lines are the same as the ones of figure 7. Parameters: $\tilde{\eta}^{-1} = 0$, $Le = 6 \times 10^{-4}$, $\boldsymbol{u}_0 = \mathbf{1}_x$ (see Table 2 for others parameters at corresponding wavelengths).

increasing topography wavelength. For 3D topography and non-traditional β-plane, the domain of Rossby-MAC waves extends to a wider range of Ro, in agreement with equation (3.4).

(d) Wave-driven stress

The boundary stress originates either from wave generation or from Ohmic dissipation. To disentangle these effects, we compare in figure 9 the stress for the asymptotic limit $Rm \gg 1$ (figure 9(a)) of weak diffusion (the stress being strictly zero for $Rm^{-1} = 0$) and for a moderate $Rm = 0.625$ (figure 9(b)). We thus investigate a 2D section of the parameter space (Ro, Al, Rm) that is different from the section explored in figures 7 and 8. At large Rm (figure 9(a)), the limit between the hydrodynamic and MHD cases corresponds to a constant Lehnert number instead of $\Lambda = 1$ for $Rm = \mathcal{O}(1)$ or lower (figures 7, 8 and 9(b)). In some parts of the space (Ro,Al), the figures 9(a) and 9(b) are identical, showing that the stress has to be attributed to wave generation only. Conversely, we find a parameter range for which the stress varies as Rm^{-1} (hatched zone), showing that it comes from Ohmic dissipation. This corresponds to the range of Rossby number delimited by equation (3.4), where MAC-Rossby waves propagate. The stress is thus dominated by Ohmic dissipation in this zone of interest for the Earth's core.

To understand better the mechanism at play in the establishment of stress, we have carried out a more detailed study of the waves arising in figure 7(d). We show in figure 10 the vertical wave numbers k_z as a function of Ro for a large interaction parameter ($RoAl^{-2} = 10$) and a fixed $Le = 0.0122$ (same as in figure 7(d)) and compare them with the solution of the theoretical dispersion relation in the diffusionless limit. We also show the relative contribution of each wave to the total tangential stress. Because curvature effects related to the β-plane are not easily visible in the real

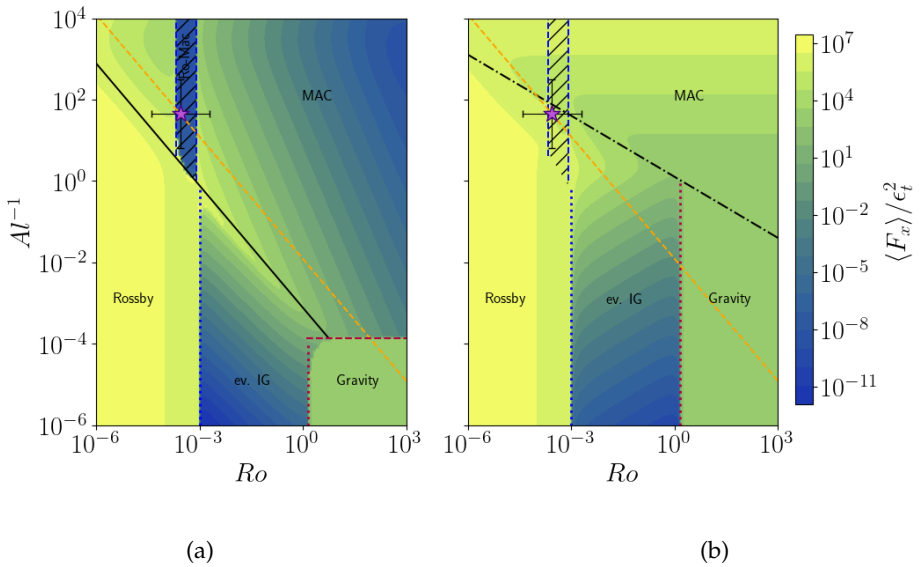

Figure 9. Normalised stress as a function of Al and Ro ($\theta = \pi/4$, $\tilde{\eta}^{-1} = 0$). The basic velocity is $\boldsymbol{u}_0 = \mathbf{1}_x$ and $\boldsymbol{b}_0 = \sin(\theta)/2\mathbf{1}_y - \cos\theta\mathbf{1}_z$, with a non-traditional β-plane, other parameters are those of table 2 for $\tilde{k}^{-1} = 5$ km. (a) ideal MHD approximation, $Rm = 10^{15}$, black solid line is $Le = 7.5 \times 10^{-4}$, delimiting the hydrodynamic and MHD zones. (b) Diffusive case, $Rm = 0.625$, dashed-dotted line is $\Lambda = 1$. Hatches correspond to the region where the stress is proportional to dissipation ($\propto Rm^{-1}$). The black dashed line shows $Le = 0.122$, for which figure 7 has been calculated. Vertical lines and symbols as in figure 7.

part of k_z 10(a), we show the imaginary part of k_z in figure 10(b). Our results superimpose almost exactly to dispersion relation MAC waves and Rossby-MAC (not shown) in figure 10(a) and 10(b) respectively. The remaining difference originates from diffusion. In figure 10(a), the stress is mainly driven by the wave of greatest k_z, except above Al given by equation (3.2). This branch consists of MAC waves since it involves all magnetic field, rotation, and stratification. Another branch is well described by the dispersion equation for Alfvén waves (purple dashed curve). It has a small $\Re(k_z)$ and contributes negligibly to the total stress. For large Al, the waves with the smallest $\Re(k_z)$ are responsible for most of the stress. Their wavenumbers obey the dispersion relation of internal waves, and the stress depends only on Fr. Overall, stratification is key in all stress mechanisms investigated here. Including β-plane (figure 10(b)), the MAC branch still carries most of the stress. The only difference is the emergence of a domain where Rossby-MAC waves propagate. Looking at figure 7(d) we see that it corresponds to a sudden drop in the stress. In this parameter range, the solution consists of a combination of MAC and Rossby-MAC waves, the MAC waves carry most of the stress but have a negligible amplitude compared to Rossby-MAC waves. Rossby-MAC waves are indeed very inefficient at driving boundary stresses and are key for this stress drop. By contrast, in the hydrodynamic limit, the Rossby waves at low Ro are very efficient in generating stress (figure 7(d)). In the supplementary figure, we also provide k_z and the relative contribution of each wave in the hydrodynamic limit.

Finally, we focus on the large stress values that are obtained at the limits of Rossby and Rossby-MAC wave domains (equations 3.3-3.4), which are too abrupt to be seen in Figure 7(d). This is illustrated in figure 11(a), which shows the normalised stress along the horizontal lines $RmAl^{-2} = 10^{10}$ in the ideal MHD limit (orange) and $RmAl^{-2} = 10^{-10}$ in the hydrodynamic limit (blue). At the frontiers of Rossby wave domains, we observe sharp increases that suggest mode resonances. Calculating the eigenmodes of our problem, we obtain free steady (MAC-) Rossby modes that can be excited by the topography-forced waves. Looking at the corresponding wavenumber (Figure 11(b)), at resonances, the wavevector is found to be perpendicular to the

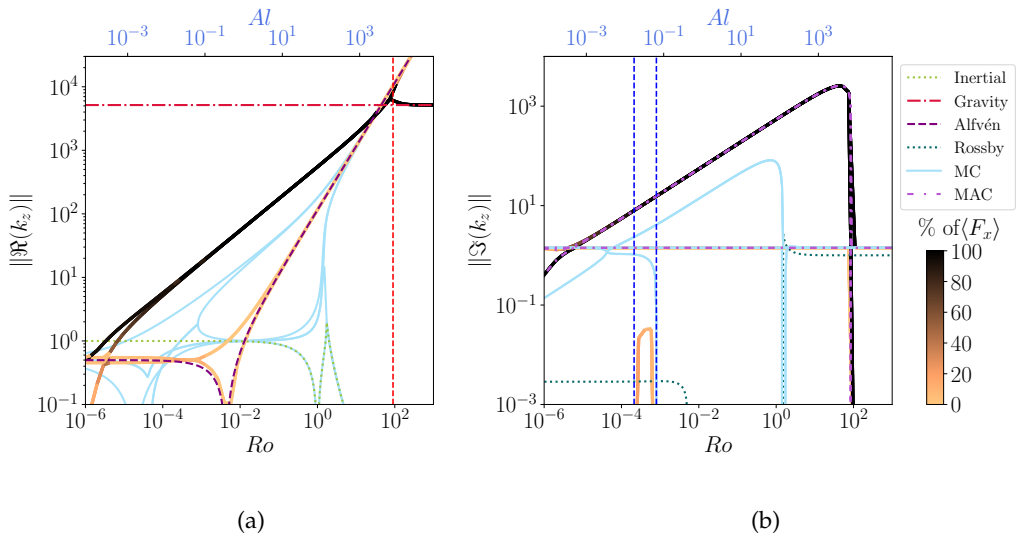

Figure 10. Absolute value of the real (a) or imaginary (b) part of the vertical wavenumbers k_z as a function of Ro. Our results are colour-coded to show the relative contribution of each k_z to the total stress. Other lines show diffusionless MHD wave dispersion relations [23]. The red vertical dashed line is equation 3.2, and the blue ones correspond to equation 3.4. Parameters: same as figure 7(d), with $RmAl^{-2} = 10^{10}$.

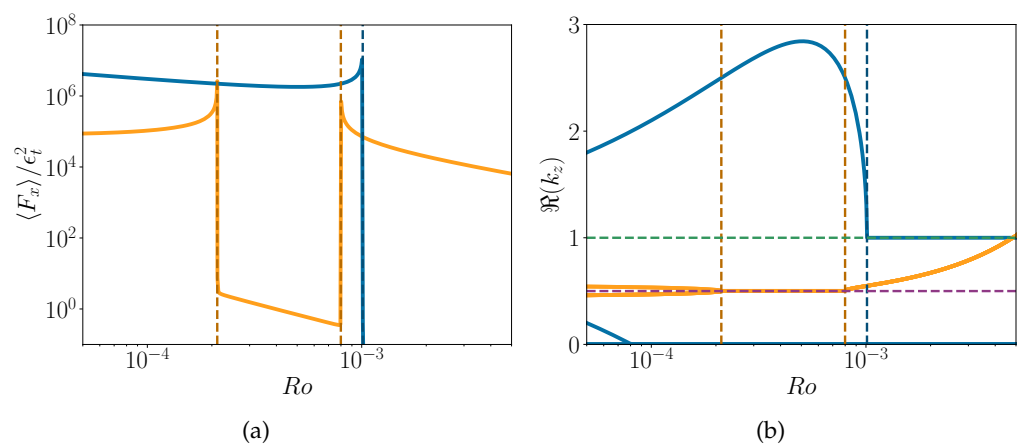

Figure 11. (a) Normalized stress vs Ro for $RmAl^{-2} = 10^{10}$ (ideal MHD, orange) and $RmAl^{-2} = 10^{-10}$ (hydrodynamic limit, blue), (b) Real part of vertical wavenumber vs Ro. Vertical lines correspond to theoretical limits for Rossby waves (equation 3.3, dashed blue) and MAC-Rossby waves (equations 3.4, dashed orange). Horizontal lines are $\boldsymbol{k} \cdot \boldsymbol{\Omega} = 0$ (green dashed line), and $\boldsymbol{k} \cdot \boldsymbol{b_0} = 0$ (purple dashed line). Parameters: same as figure 7(d).

rotation vector in the hydrodynamic case (green dashed line) and perpendicular to the magnetic field (pink dashed line) in the ideal MHD limit (this helped us to find equation 3.4).

4. Discussion

We now discuss how we can extend our model to planetary-relevant geometries and relate our work to previous studies. The force balance we have investigated is only possible with mass

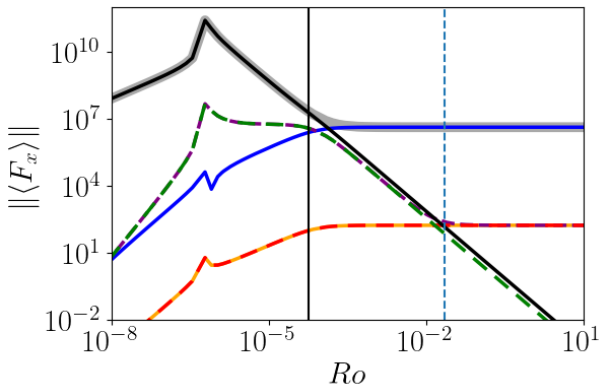

Figure 12. Magnitude of Lorentz (blue/purple), Coriolis (black/green) and $(\boldsymbol{u}\cdot\nabla)\boldsymbol{u}$ (orange/red) forces as a function of Ro, calculated at the surface (through the bumps, see equations 4.1, solid lines) and in the fluid interior (dashed). The grey line is the boundary pressure stress. The solid vertical line is $\Lambda = 1$, the dashed blue one is $Le = 1$. Parameters are those of table 2 for $\tilde{k}^{-1} = 100$ km, $\theta = 0$, $\tilde{\eta}^{-1} = 0$. Calculations are for a ridge topography within an f-plane approximation.

fluxes and electrical currents at infinity, which cannot occur in bounded geometries. Our second-order results enable us to calculate these fluxes in the bulk and not only at the boundary. We also investigate how to extend the results obtained for semi-infinite fluid to a duct geometry. We can thus study modes that are not confined to the wall vicinity. A short subsection is devoted to the effects that arise when the solid domain is electrically conducting. Finally, the scale dependence of the topographic stress is discussed for the core-mantle coupling.

(a) Electric currents and flows at infinity

We have been able to calculate mean stresses, that are not balanced by an inertia term $\partial_t \boldsymbol{u}$. Similarly, we find that the magnetic stress on the fluid side is non-zero, although the mantle is electrically insulating. We interpret these results as a limitation of periodic box models: Coriolis and Lorentz mean forces balance the mean pressure force. They arise from the mean flux of mass and electrical currents at infinity. The linear solution induces second-order mass fluxes and electric currents across the bumps [12] as

$$\mathcal{U} = \iint_S u_y(x,z)\,\mathrm{d}S = \int h(x) u_y(x,0)\,\mathrm{d}x, \qquad \mathcal{J} = \iint_S j_y(x,z)\,\mathrm{d}S = \int h(x) j_y(x,0)\,\mathrm{d}x, \tag{4.1}$$

where S is a plane of constant y, and $\boldsymbol{j}$ the electrical current density $\nabla \times \boldsymbol{b}$. These fluxes yield mean Coriolis $2Ro^{-1}\Omega_z \mathcal{U}$ and Lorentz forces $b_{0_z}\mathcal{J}$. Since we calculate second-order solutions, we are able to obtain the fluxes of mass and current in the fluid interior and compare them with the fluxes at the surface (figure 12, where $\theta = 0$ and a ridge topography are considered following [12]). First, the Lorentz, Coriolis, and inertial ($(\boldsymbol{u}\cdot\nabla)\boldsymbol{u}$) forces in the interior cancel out. Second, the $(\boldsymbol{u}\cdot\nabla)\boldsymbol{u}$ contribution at the surface exactly balances its contribution in the interior as a consequence of the no-penetration boundary condition and impressibility. Finally, we find that for $\Lambda < 1$ the Coriolis force is stronger than the Lorentz force and vice versa for $\Lambda > 1$. In both cases, the surface force predominates. Physically, this force tends to oppose the differential velocity between the fluid and the solid. We need to include in our model the feedback of the force on the fluid and solid velocities. Similarly, there will be a retroaction of the electrical field on the ambient magnetic field.

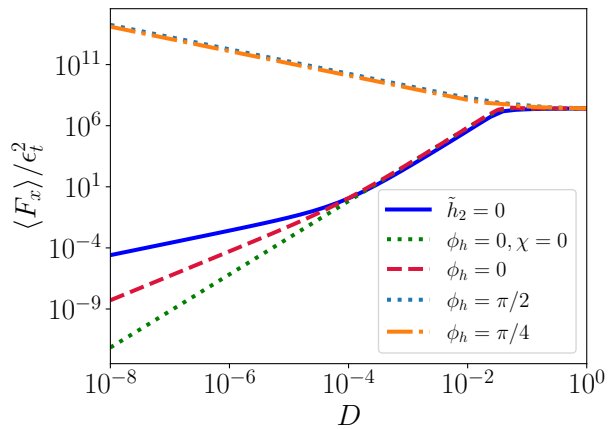

Figure 13. Normalized stress as a function of the distance between the two boundaries D, for different bottom boundary shapes ($Ro = Fr = 1.37 \times 10^{-5}$, $\theta = \pi/4$, $\tilde{\eta}^{-1} = 0$). The basic velocity is $\boldsymbol{u}_0 = \mathbf{1}_x$ and $\boldsymbol{b}_0 = \sin(\theta)/2\mathbf{1}_y - \cos\theta \mathbf{1}_z$. The top boundary is $h = \epsilon_t \cos x$, and the bottom boundary is $h_2 = \epsilon_t \tilde{h}_2 \cos(x + \phi_h) - D$. When not specified otherwise, $\tilde{h}_2 = 1$ and $\chi = 0.0286$. Other parameters are the ones of Table 2 for $\tilde{k}^{-1} = 100$ km.

(b) Duct geometry

In his 1998 paper, Braginsky [11] proposed a model of a stratified layer at the top of the core. To mimic a sharp density jump between this layer and the well-mixed convective bulk, he considered a solid second boundary at this transition. Even if this does not model perfectly a two fluids interface, this avoids the problems that can be encountered in a semi-infinite domain, when the waves propagate further than the fluid layer we want to model, or even over distances about the core radius. Besides, such a second boundary is relevant to laboratory experiments.

Therefore, we have introduced a second solid boundary in our model. In figure 13 we show the stress as a function of the distance D between the two boundaries. As expected, the second boundary does not affect the stress when D is large enough (here for a fluid layer thicker than 10 km). Conversely, the results are more complex for a thinner fluid layer. Focusing on $D \ll 1$, the stress on the top boundary vanishes when the topographies are in phase whereas it diverges otherwise (a second flat boundary being seen as in phase),

$$\langle F_x \rangle / \epsilon_t^2 \propto f_0 D^{-1} + f_1 D + f_2 D^2 + \mathcal{O}(D^3), \tag{4.2}$$

for $h/\epsilon_t = \cos x$ and $h_2/\epsilon_t = \tilde{h}_2 \cos(x + \phi_h) - D$. Taylor expansion coefficients (4.2) for $D \ll 1$ scale as $f_0 \propto \tilde{h}_2 \sin(\phi_h)/(\chi - \chi_c)$, $f_1 \propto (1 - \tilde{h}_2)$ and $f_2 \propto \chi_c \chi/(\chi - \chi_c)$, with χ_c the solution of equation (3.3). Interestingly, the coefficients f_0 and f_2 can be either positive or negative according to the value of χ. This corresponds to the presence or not of MAC-Rossby waves. This differs from the semi-infinite case, where the pressure on the fluid side is always opposed to the basic flow. When the two boundaries are in phase ($\phi_h = 0$), axially invariant geostrophic motions are part of the solution. They have been shown in another context to be ineffective in generating pressure stress [24].

(c) Electrically conducting solid

In this section, we get closer to geophysical applications. To do that, we will consider a conducting solid to model the Earth mantle, and variations with the latitude of Ω and $\boldsymbol{b_0}$. Finally, we cover a spherical surface with local planes and integrate them to obtain global quantities. To localise magnetic perturbation in the mantle close to the surface, we consider an oscillating flow $\boldsymbol{u}_0 = \sin\theta \cos(\omega t)\mathbf{1}_x$, corresponding to a solid body rotation in spherical geometry. Buffett

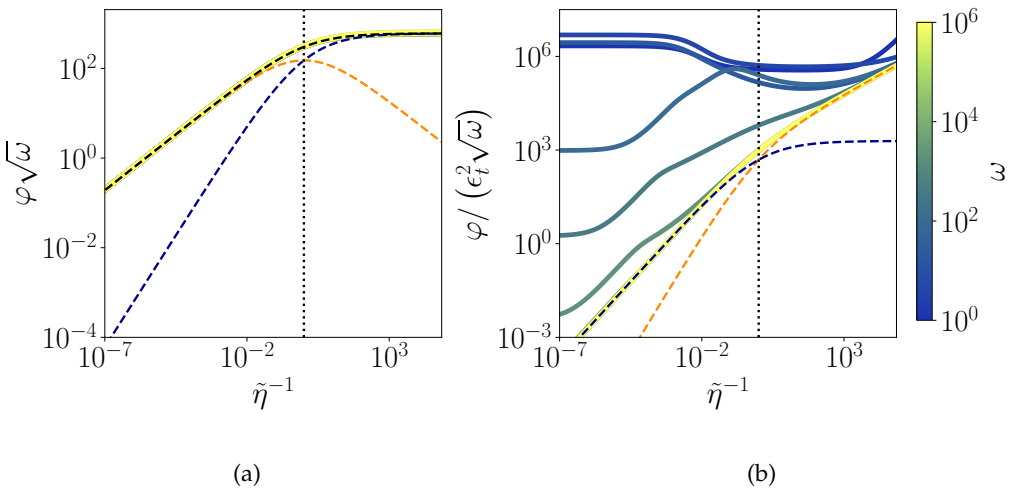

Figure 14. Normalised mean dissipation as a function of η^{-1}, at order in topography $m=0$ (a), corresponding to a flat boundary, and $m=2$ (b). $m=1$ terms are identically zero. Dissipation is calculated for a set of ω (colour), with $\boldsymbol{u}_0=\sin\theta\cos(\omega t)\mathbf{1}_x$. The vertical dotted line is $\tilde{\eta}^{-1}=1$. Dashed lines are the theoretical results for total (black), fluid (blue) and solid (orange) dissipation, after the results of Buffett (2010) [14] in figure (a), and after our results at $\omega=10^6$ in figure (b). Parameters : $\boldsymbol{b}_0=\sin(\theta)/2\,\mathbf{1}_y-\cos\theta\mathbf{1}_z$, $\boldsymbol{\Omega}$ is from equation (2.4) and $\theta=\pi/4$. Other parameters are those in Table 2 for $\tilde{k}^{-1}=100$ km.

(2010) suggested combining topographic and electromagnetic coupling to explain the out-of-phase component of annual nutation [14]. He used total dissipation to estimate the coupling strength. We calculate the dissipation φ as an integral of $Rm^{-1}\,\tilde{\eta}j^2$ in the solid and $Rm^{-1}\,j^2$ in the fluid.

Considering first the order $m=0$ corresponding to a flat boundary, we calculate the dissipation due to the electromagnetic coupling as a function of frequency (figure 14(a)). All curves superimpose because the dissipation scales as $\omega^{-1/2}$. Our results agree in the whole range with predictions obtained from equations (19) and (24) of Buffett (2010) [14], which provides the mean dissipation in the solid (dashed orange), in the fluid (dashed blue) and their sum (dashed black). The topographic coupling leads to an additional dissipation (figure 14(b)), which scales as ϵ_t^2. In the limit $\omega\gg1$, the dissipation scales as $\mathcal{O}(\omega^{1/2})$. It occurs mainly in the solid for $\eta>1$ and in the fluid otherwise. The vertical wave numbers k_z obtained vary as $\omega^{1/2}$ for $\omega\gg1$. The stress scales as k_z, which explains the observed scaling $\varphi\propto\sqrt{\omega}$. However, the dissipation cannot increase indefinitely with ω and, in our model, it is limited by the bound on acceptable $\epsilon_t<\mathcal{O}(k_z^{-1})$. Therefore, the dissipation remains bounded by $\mathcal{O}(\omega^{-1/2})$ in our model.

(d) Scale dependence of the core-mantle topographic stress

Combining β-plane and 3D topographic effects, we can span a wide range of length scales, from the viscous boundary layer thickness to the Earth's core radius. For a given height of the topography, figure 15 shows that the topographic mean stress varies in a non-trivial way over several decades. The sharp variation at 30 km corresponds to the transition between Rossby-MAC and MAC waves given by equation (3.4). The mean normalised stress $\langle\tilde{F}_x\rangle/\tilde{h}_0^2$ keeps the same order of magnitude from 10 m to 50 km. Our results can be combined with seismological estimates of Earth's core topography [25–27] to provide the global torque on the core. Figure 15 gives the tangential stress for an illustrative but realistic example of core-mantle topography, which increases with the horizontal length scale $l=2\pi\tilde{k}_x^{-1}$ until $l=300$ km. We find that the peak in the stress coincides with the value of l for which the topography amplitude stops increasing.

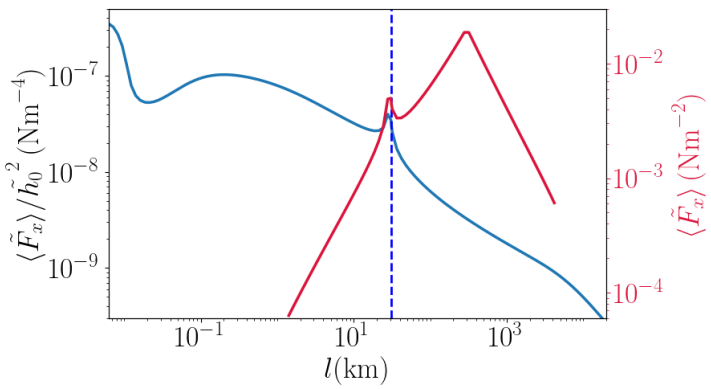

Figure 15. Topographic (dimensional) mean stress $\langle\tilde{F}_x\rangle/\tilde{h}_0^2 = \rho_r\tilde{U}^2\langle F_x\rangle/\tilde{h}_0$ normalised by the topography $\tilde{h}_0 = \epsilon_t/\tilde{k}_x$ (blue), or for a CMB topography model (red) as a function of the topography wavelength $l = 2\pi\tilde{k_x}^{-1} = 2\pi\chi R$ for the Earth's core parameters. Parameters: $h = \epsilon_t\cos x\cos y$, $\rho_r = 10^4$ kg.m^{-3}, $\tilde{U} = 10^{-4}$ m.s^{-1}, $B = 5\times10^{-4}$ T, $\eta = 0.8$ m^2.s^{-1}, $R = 3486$ km, $\Omega_0 = N = 7.29\times10^{-5}$ rad.s^{-1}, $\theta = \pi/4$, $\tilde{\eta}^{-1} = 0$. Topography model for the Earth's CMB [25–27]: $\tilde{h}_0 = 0.022l^{0.83}$ for $l < 300$ km, and $\tilde{h}_0 = 28l^{-0.42}$ otherwise (with l and $\tilde{h}_0$ in km).

5. Conclusion and future works

We have developed a generic approach to calculate efficiently the flows over a bumpy boundary, in various cases and within parameter ranges that were previously difficult to achieve. We have reproduced the linear results of the literature and went further by adding weakly non-linear corrections, which enabled us to alleviate several previous limitations. We have investigated the physical effects at play in the topographic stress and characterised the fluid waves involved, highlighting regime changes and non-trivial variations. Notably, we have shown the uttermost importance of considering 3D topographies and effects of curvature that yield results qualitatively different from the ridge topography. We have explored inviscid laminar regimes, although much remains to be done on hydromagnetic topographic coupling. For the oceans or the atmosphere, turbulence and flow separation can drastically change the stress on the wall. Even if we have included weakly non-linear terms, they do not account for these effects, which can only be managed by DNS or laboratory experiments (but for parameters far from planetary core ones).

While we have made considerable efforts to better model global geometry effects, some limitations remain, associated with periodic box models. In such steady models, Jault (2020) showed for instance that, while mean pressure forces balance with Coriolis and Lorentz mean forces, the flow linear solution forces second-order mass fluxes and electric currents between the bumps. Our full-order two calculations are required to provide the correct balance of these mean fluxes. The problem at infinity remains but could be solved by relaxing the steadiness assumption. One possible way forward consists of coupling a local estimation of the instantaneous stresses at the boundary (knowing $\mathbf{u}_0$ and $\mathbf{b}_0$ as done in this study) with a model (possibly axially symmetric) in spherical geometry for the time evolution of $\mathbf{u}_0$ and $\mathbf{b}_0$ as a function of the surface stresses.

The different spatial missions also provide geodetic and rotation data on other planetary bodies, showing that they also host liquid layers such as subsurface oceans [28–32]. Efforts have already been made to infer the geometry and the dynamic of these oceans and their coupling with the solid layers. These subsurface oceans probably have interesting topographic coupling effects to explore, which can be investigated with our model.

Data Accessibility. The code "ToCCo" for Topographic Coupling at the Core boundaries, is available at gitlab.com/monvilre/tocco

Authors' Contributions. Advised by D.C. and D.J., R.M. developed the code "ToCCo" during his PhD. D.C. conducted the COMSOL simulations. R.M. produced the results, that were discussed by all authors, and drafted the paper. All authors contributed to the writing of the final version and approved the submission.

Competing Interests. The authors declare that they have no competing interests.

Funding. This work received funding from the European Research Council under the European Union's Horizon 2020 research and innovation programme (THEIA project, grant agreement no. 847433). ISTerre is part of Labex OSUG@2020 (ANR10 LABX56).

Acknowledgements. We acknowledge Jérémie Vidal for constructive discussions both on the methods and the results. Figures were produced using Matplotlib [33] using scientific colourmaps [34] designed to prevent visual distortion of the data and exclusion of readers with colour-vision deficiencies

References

1. Taylor GI. 1916 Skin friction of the wind on the earth's surface. *Proceedings of the Royal Society of London. Series A, Containing Papers of a Mathematical and Physical Character* **92**, 196–199.
2. Reynolds O. 1883 XXIX. An experimental investigation of the circumstances which determine whether the motion of water shall be direct or sinuous, and of the law of resistance in parallel channels. *Philosophical Transactions of the Royal society of London* **174**, 935–982.
3. Baines PG. 2022 *Topographic effects in stratified flows*. Cambridge university press.
4. Legg S. 2021 Mixing by oceanic lee waves. *Annual Review of Fluid Mechanics* **53**, 173–201.
5. Finlay CC. 2008 Course 8 Waves in the presence of magnetic fields, rotation and convection. In *Les Houches* pp. 403–450. Elsevier.
6. Gillet N, Jault D, Canet E, Fournier A. 2010 Fast torsional waves and strong magnetic field within the Earth's core. *Nature* **465**, 74–77.
7. Gillet N, Gerick F, Jault D, Schwaiger T, Aubert J, Istas M. 2022 Satellite magnetic data reveal interannual waves in Earth's core. *Proceedings of the National Academy of Sciences* **119**, e2115258119.
8. Mathews PM, Herring TA, Buffett BA. 2002 Modeling of nutation and precession: New nutation series for nonrigid Earth and insights into the Earth's interior. *Journal of Geophysical Research: Solid Earth* **107**, ETG–3.
9. Roberts PH, Aurnou JM. 2012 On the theory of core-mantle coupling. *Geophysical & Astrophysical Fluid Dynamics* **106**, 157–230.
10. Hide R. 1969 Interaction between the Earth's liquid core and solid mantle. *Nature* **222**, 1055–1056.
11. Braginsky SI. 1998 Magnetic Rossby waves in the stratified ocean of the core, and topographic core-mantle coupling. *Earth, Planets and Space* **50**, 641–649.
12. Jault D. 2020 Tangential stress at the core–mantle interface. *Geophysical Journal International* **221**, 951–967.
13. Glane S, Buffett B. 2018 Enhanced Core-Mantle Coupling Due to Stratification at the Top of the Core. *Frontiers in Earth Science* **6**.
14. Buffett BA. 2010 Tidal dissipation and the strength of the Earth's internal magnetic field. *Nature* **468**, 952–954.
15. Dellar PJ. 2011 Variations on a beta-plane: derivation of non-traditional beta-plane equations from Hamilton's principle on a sphere. *Journal of Fluid Mechanics* **674**, 174–195.
16. Acheson D. 1975 On Hydromagnetic Oscillations within the Earth and Core–Mantle Coupling. *Geophysical Journal International* **43**, 253–268.
17. Rossby CG. 1939 Relation between variations in the intensity of the zonal circulation of the atmosphere and the displacements of the semi-permanent centers of action. *J. mar. Res.* **2**, 38–55.
18. Grimshaw RHJ. 1975 A note on the β-plane approximation. *Tellus* **27**, 351–357.
19. Buffett BA. 2021 Conditions for turbulent Ekman layers in precessionally driven flow. *Geophysical Journal International* **226**, 56–65.
20. Meurer A, Smith CP, Paprocki M, Čertík O, Kirpichev SB, Rocklin M, Kumar A, Ivanov S, Moore JK, Singh S et al.. 2017 SymPy: symbolic computing in Python. *PeerJ Computer Science* **3**, e103.

21. Johansson F et al.. 2013 *mpmath: a Python library for arbitrary-precision floating-point arithmetic (version 0.18)*. `http://mpmath.org/`.
22. Athanassiadou M. 2003 Wave and form drag: their relation in the linear gravity wave regime. *Tellus A: Dynamic Meteorology and Oceanography* **55**, 173–180.
23. Salhi A, Baklouti F, Godeferd F, Lehner T, Cambon C. 2017 Energy partition, scale by scale, in magnetic Archimedes Coriolis weak wave turbulence. *Physical Review E* **95**, 023112.
24. Gerick F, Jault D, Noir J, Vidal J. 2020 Pressure torque of torsional Alfvén modes acting on an ellipsoidal mantle. *Geophysical Journal International* **222**, 338–351.
25. Koelemeijer P. 2021 9. In *Toward Consistent Seismological Models of the Core–Mantle Boundary Landscape*, pp. 229–255. American Geophysical Union (AGU).
26. Garcia R, Souriau A. 2000 Amplitude of the core–mantle boundary topography estimated by stochastic analysis of core phases. *Physics of the Earth and Planetary Interiors* **117**, 345–359.
27. Mancinelli N, Shearer P. 2016 Scattered energy from a rough core-mantle boundary modeled by a Monte Carlo seismic particle method: Application to PKKP precursors. *Geophysical Research Letters* **43**, 7963–7972.
28. Van Hoolst T, Baland RM, Trinh A, Yseboodt M, Nimmo F. 2020 The librations, tides, and interior structure of Io. *Journal of Geophysical Research: Planets* **125**, e2020JE006473.
29. Nimmo F, Hamilton DP, McKinnon WB, Schenk PM, Binzel RP, Bierson CJ, Beyer RA, Moore JM, Stern SA, Weaver HA. 2016 Reorientation of Sputnik Planitia implies a subsurface ocean on Pluto. *Nature* **540**, 94–96.
30. Hoolst TV, Baland RM, Trinh A. 2016 The diurnal libration and interior structure of Enceladus. *Icarus* **277**, 311–318.
31. Čadek O, Tobie G, Van Hoolst T, Massé M, Choblet G, Lefèvre A, Mitri G, Baland RM, Běhounková M, Bourgeois O. 2016 Enceladus's internal ocean and ice shell constrained from Cassini gravity, shape, and libration data. *Geophysical Research Letters* **43**, 5653–5660.
32. Baland RM, Tobie G, Lefèvre A, Van Hoolst T. 2014 Titan's internal structure inferred from its gravity field, shape, and rotation state. *Icarus* **237**, 29–41.
33. Hunter JD. 2007 Matplotlib: A 2D graphics environment. *Computing in Science & Engineering* **9**, 90–95. (10.1109/MCSE.2007.55)
34. Crameri F. 2018 Scientific colour maps. *Zenodo* **10**.